MECSOL 2019 - Proceedings of the 7th International Symposium on Solid Mechanics,
V. Tita, A. Ferreira, M.L. Ribeiro, A. Vieira and A.T. Beck (Editors), ABCM, Sao Carlos, SP, Brazil, April 15th to 17th, 2019

Tridimensional Dynamic Compression of Flexible Risers

Fernanda Rizzi Gama da SIlva [1] and Juan Pablo Julca Avila [2]

[1] Federal University of ABC, fernanda.rizzi@aluno.ufabc.edu.br

[2] Federal University of ABC, juan.avila@ufabc.edu.br

Abstract: The present work aims to study the kink formation and dynamic compression on risers, which are strictly correlated to the wave motion and sea current. Those phenomena can seriously affect the riser structure leading to failure and consequently loss of its functionality. For those reasons, a parametric study will be conducted on the behavior of a catenary flexible riser submitted to heave and roll motions due to regular and irregular waves. The models will be analyzed using ABAQUS, a software based on the finite element method.

Keywords: catenary riser, flexible riser, finite element method, dynamic compression, kink formation

INTRODUCTION

The offshore industry has increased over the years due to the development of new technologies of petroleum extraction in deep waters (Neto, 2012). One of those is known as catenary flexible risers, which are free-hanging multi-layered structures that present low tension levels on their touchdown zone (TDZ). The risers can be connected to floating platforms known as FPSO (Floating Production, Storage and Offloading), which are ships with great oil storage capacity having six degrees of freedom: surge, sway, heave, roll pitch and yaw. In this study, just roll (rotation about longitudinal axis) and heave (vertical translation) motions are considered.

As a consequence of the riser configuration and the platform heave motion due to wave behavior, the tension levels along the structure can decrease, and it is possible that the touchdown zone experiences compressive loads. According to Amarante (2015), it occurs when the Euler's critical load is exceeded, and the riser cannot support the external loads anymore, leading to global buckling. The energy not accumulated is transferred to the structure as compression waves, which travels from the touchdown point (TDP) to the top of the riser. In addition, flexible risers over negative tension can deflect out of plane, moving axially and laterally. Another important phenomenon observed in flexible risers is the kink formation, which is caused mainly due to torsion of the structure. As stated by Koloshkin (2016), when the effective tension of the riser cannot support the roll motion, the torsion energy is transformed into bending energy causing kink formation on the touchdown zone. Thus, when those phenomena are experienced at the same time, the riser can present large deflections and curvatures that can cause failure of the structure.

Many studies have been conducted on this area, and the one developed by Myazaki and Kondo (1997) focus on the kink formation on a straight beam. Mainly, their work discusses the behavior of a beam fixed in one end and submitted to shortening and torsion in the other one. When the structure experiences end-shortening load before torsion, it buckles in its plane. On the other hand, when torsion is imposed before shortening, the beam buckles out of its plane. Hence, Myazaki and Kondo (1997) concluded that three solutions are possible when tension is imposed after the loop is formed. These solutions are known as non-kinking, semi-kinking, and kinking. The non-kinking happens when the loop is undone, the semi-kinking occurs when a kink is formed but there is no self-contact of the beam, and finally the kinking solution happens when kink is formed and the beam experiences self-contact.

An important study related to dynamic compression, was developed by Ribeiro, Roberi and Mourelle (1998), which analyses an amount of factors that can affect buckling during compression. It was said that the platform motion, velocity and direction of current, top angle inclination and hydrodynamic dampers such as drag coefficient and current velocity, have a huge effect on the behavior of the structure. According to Ribeiro, Roberi and Mourelle (1998), the magnitude of compression at the touchdown point is often increased when the current velocity and the drag coefficient are small.

Therefore, the actual work aims to discuss the behavior of catenary flexible risers submitted to heave and roll motion due to regular ad irregular waves in order to analyze the kink formation and dynamic compression phenomena.

FINITE ELEMENT MODEL

The Finite Element Method is a numerical method widely used in the solution of engineering problems, which determines an approximate solution for partial differential equations by the structure discretization in several elements. The riser and the seabed were implemented using Abaqus which is based on this method.

Riser Discretization

The riser was discretized in 0.1 m elements at the TDZ and 1 m far from this critical zone. Figure 1 shows the element chosen to discretize the riser, known as B31. This is a 12 degrees of freedom, 2-node linear 3D beam element, involving bending, stretching, twisting and shearing deformation (Sun and Li, 2012).

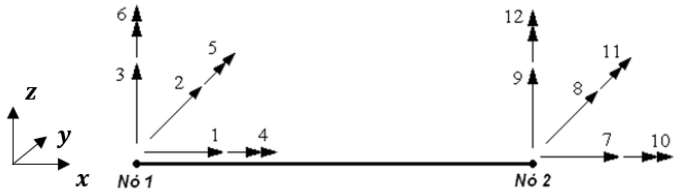

Figure 1 – Master and slave interfaces

The stiffness matrix of the element results from the sum of the elastic stiffness matrix ($\boldsymbol{K_E}$) and the geometric stiffness matrix ($\boldsymbol{K_G}$) as shown in Eq. (1) (Takafuji, 2010).

$$\boldsymbol{K = K_E + K_G} \tag{1}$$

The total mass matrix is represented by the mass matrix ($\boldsymbol{M}$) and the added mass matrix ($\boldsymbol{M_a}$), as shown in Eq. (2).

$$\boldsymbol{M_T = M + M_a} \tag{2}$$

Finally, the detailed stiffness and mass matrices for the element can be found in Appendix.

Riser-Seabed Contact

The seabed was considered as an Analytical Rigid Surface in Abaqus tied to a reference point. The contact between the seabed and the riser was given by two interfaces known as master (seabed) and slave (riser) shown in Fig. 2. Once the slave and the master nodes are not coincident, the slave points must not penetrate into the master area delimited by its nodes (Litewka, 2010).

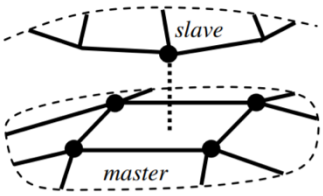

Figure 2 – Master and slave interfaces. (Litewka, 2010)

Two restrictions must be taken into account. The first one is related to the penetration of the riser into the seabed, which is not allowed as described in Eq. (3) (Neto, 2012).

$$g_N \geq 0 \tag{3}$$

where g_N is the gap function given by $g_N = (\boldsymbol{x_2} - \boldsymbol{x_2}).\boldsymbol{n_1}$, $\boldsymbol{x_1}$ and $\boldsymbol{x_2}$ are position vectors of the master and slave interfaces respectively and $\boldsymbol{n_1}$ is the normal direction.

The second restriction is given in the tangential direction, when one interface slides over the other (Eq. (4)).

$$\boldsymbol{g_T} = g_{a_1}\boldsymbol{a_1} + g_{a_2}\boldsymbol{a_2} \tag{4}$$

where $\boldsymbol{g_T}$ is the tangential gap function, $\boldsymbol{a_1}$and $\boldsymbol{a_2}$ are vectors tangential to the master surface and orthogonal between each other. If there is no sliding between the interfaces $g_{a_1} = 0$ and $g_{a_2} = 0$.

To impose this behavior, the penalty method was applied. This method imposes contact by analyzing the violated restrictions and applying normal and tangential forces (Neto, 2010). The normal behavior is presented by Eq. (5).

$$f_N = \epsilon_N g_N \tag{5}$$

where ϵ_N is the penalty parameter that regulates the increase in the normal force rate. When sliding is not considered, the tangential behavior is given by Eq. (6), whereas for the case in which sliding is considering, Eq. (7) is used (Neto, 2012).

$$f_T = \epsilon_T g_T \tag{6}$$

$$f_T = \mu |f_N| \frac{g_T}{||g_T||} \tag{7}$$

Figure 2-a shows that if the normal force is increased, less penetration is going to be observed. For the tangential behavior, Fig. 2-b shows that when the tangential gap is zero, there is no sliding between the interfaces. Also, the friction force is limited. When these values are reached, the force is constant and sliding occurs (Neto, 2012).

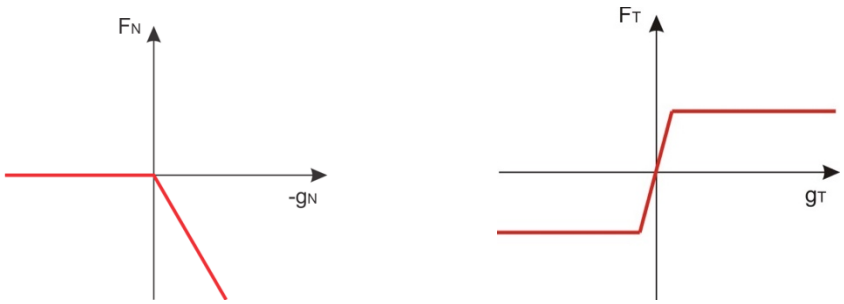

(a) Normal behavior (b) Tangential behavior

Figure 2 – Master and slave interfaces. (Neto, 2012)

REGULAR AND IRREGULAR WAVES

The sea behavior can be simplified by regular waves in ideal situations. To implement them, sinusoidal waves were used as shown in Eq. (8) (Koloshkin, 2016).

$$\eta(x,t) = \eta_0 \sin(\omega t + \varphi) \tag{8}$$

where η_0 is the wave amplitude in meters, $\omega = \frac{2\pi}{T}$ is the angular frequency in rad/s, where T is the wave period and φ is the fase angle. In many cases, this simplification can not be adopted, once the waves show random and complex characteristics. For this reason, the Person-Moskowitz (Fig. 5) energy density spectrum, defined by Eq. (9), was used to describe the irregular wave shapes based on their energy and frequency (Yasseri et al., 2014). The sea state is characterized by two main parameters known as mean-zero crossing period (T_z) and significant wave height (H_s). The mean zero crossing period is defined by the zero up and zero down crossing period, and the significant wave height is defined as the average of the highest 1/3 of waves measured from trough to crest.

$$S(\omega) = 124.2 \frac{H_s^2}{T_z^4} \omega^{-5} e^{-496/(T_z\omega)^4},\ 0 < \omega < \infty \tag{9}$$

where S is the energy.

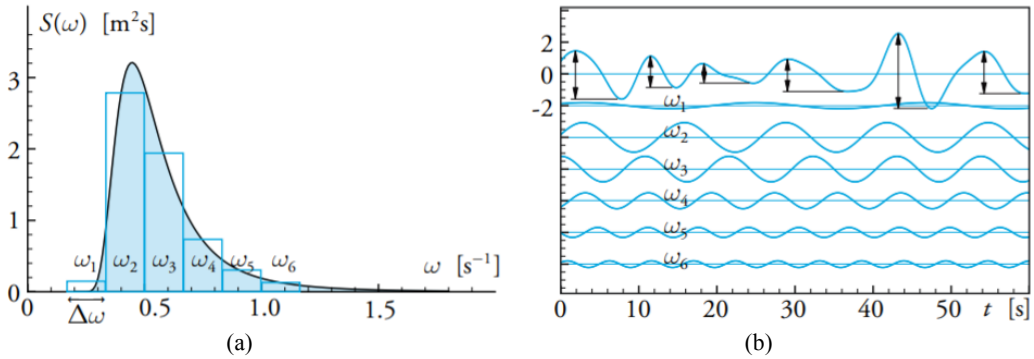

(a) (b)

Figure 5 – Wave spectra and its regular waves. Source (Yasseri et al., 2014).

The wave spectrum is divided into small frequencies, and each piece of it represents a regular wave. Then, the superposition principle is applied, and the regular waves are combined to each other in random phase. Finally, the amplitude of each wave component is given by Eq. (10).

$$a_i = \sqrt{2 \int_{\omega_i+0.5\Delta\omega}^{\omega_i+0.5\Delta\omega} S(\omega) d\omega} \tag{10}$$

The irregular wave components data used in this work can be found in Appendix. After the superposition of the components, we get the wave profile shown graphically in Fig. 6.

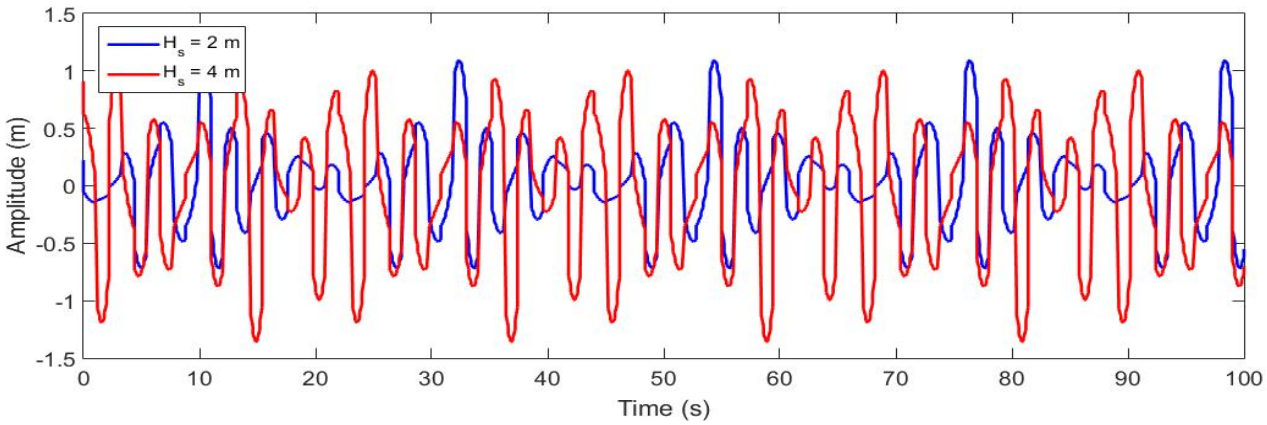

Figure 6 – Irregular wave profile for $T_z = 7\ s$

STATIC EQUILIBRIUM CONFIGURATION

The simulation can be divided into two parts, the static and dynamic ones. The static equilibrium of the riser was achieved by a sequence of two steps as follows in Fig. 7. The first step consisted in applying the effective weight of the riser, while in the second one, the end of the riser was submitted to horizontal and vertical displacements concomitantly.

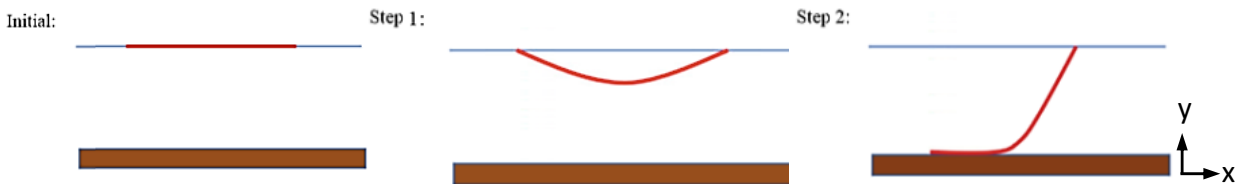

Figure 7 – Steps to achieve the catenary configuration

The configuration was achieved by applying the equations of a catenary cable, which gave the parameters in Tab. 1. The material properties of the structures are given in Tab. 2. Once the catenary parameters were found and the material properties defined, the riser was divided into elements of 1 m, while the seabed was defined as a rigid surface.

The time step was set as automatic to achieve the convergence, so that the smaller time step obtained was in the order of 10^{-6} s for the static simulation.

Table 1 – Catenary Parameters (Koloshkin, 2016)

Top angle inclination (α)	89.6°	**Top tension (T)**	141378.48 N
Catenary length (S)	1007 m	**TDP tension (T_0)**	986.4 N
Flowline length (l)	600 m	**Displacement in x-direction**	967.25 m
Effective weight (W_s)	140.3 kg	**Displacement in y-direction**	1000 m

Table 2 – Material Properties (Koloshkin, 2016)

Axial Stiffness (EA)	409 MN
Bending Stiffness (EI)	5.03 kNm^2
Torsion Stiffness (GJ)	1 MNm^2

After those static steps, the riser achieved its equilibrium as shown in Fig. 8, and the friction coefficients ($\mu_x = 0.4\ and\ \mu_z = 1$) were applied.

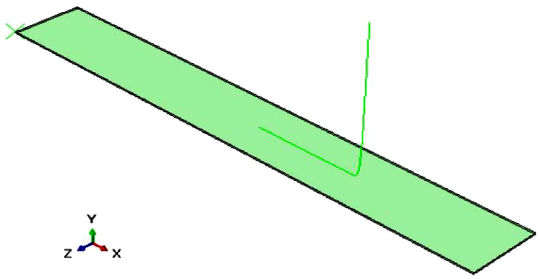

Figure 8 – Catenary equilibrium configuration

VALIDATION

Neto (2010) studied the behavior of a flexible riser under rotation on its end, and different friction coefficients for the seabed ($\mu = 0, \mu = 0.4\ and\ \mu = 1$). In his study he found a maximum moment of 5 kNm for the three cases.

The same simulations were done to validate the riser. It was applied a rotation ($\theta_x = 12\ rad$) in the top end of the riser during 20 s by a dynamic analysis. The time step was set as automatic, and its minimum value was in the order of 10^{-2} s.

From Fig. 9, it is possible to visualize that all cases show almost the same curve. The maximum torsion moment found was about 5.6 kNm. The difference between Neto (2010) and this simulation done in Abaqus is given by dynamic effects related to the 20 s ramp chosen for the dynamic simulation. According to Koloshkin (2016), these effects can be reduced by increasing the ramp.

An additional case was simulated where the friction moment is different in x-direction and z-direction. This is going to be the case studied further in this paper.

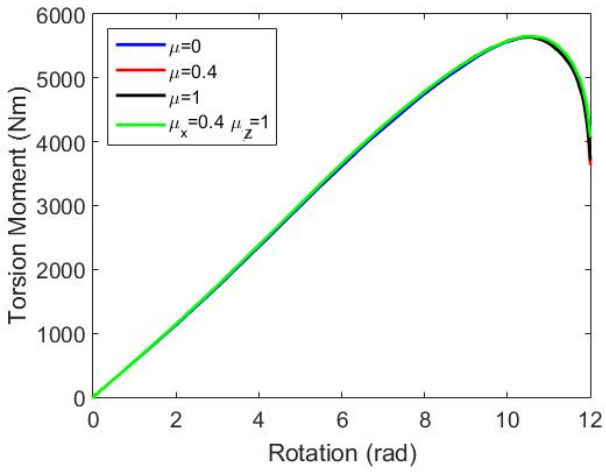

Figure 9 – Torsion Moment

DYNAMIC RESULTS

Regular heave motion

The first simulation considered a 100 s dynamic step, in which was imposed a regular heave of 7 s period and amplitude of 2 m. The time step was set as automatic, and the smaller time step was found to be in the order of 10^{-3} s . The simulation was conducted in an environment given by the data of Tab. 3.

Table 3 – Simulation data (Neto, 2012)

Hydrodynamic coefficients	
Tangential Drag Coefficient	0.1
Normal Drag Coefficient	1
Normal Mass Coefficient	1
External Diameter	0.12 m

Two cases were implemented, one considering a linear velocity profile of -0,5 m/s for current as shown in Fig. 10, and the other one, not considering sea current.

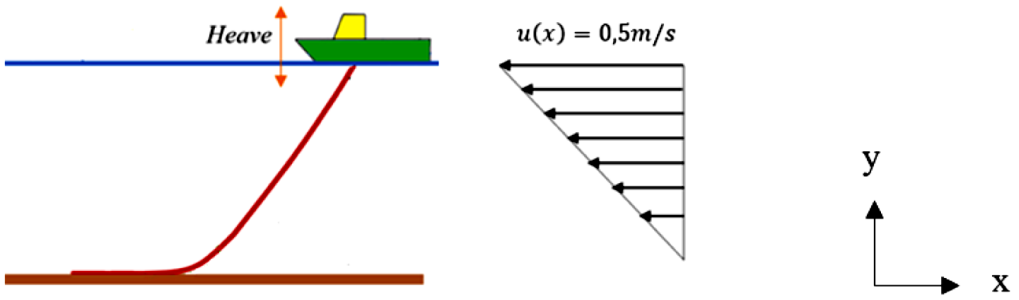

Figure 10 – Linear sea current velocity profile

The results of the simulation are shown in Fig. 11. Overall, the displacement curves have similar behaviors, which in the simulation including current presented some deviations. In contrast to that, the tension curve for the current case showed larger peaks in the first twenty seconds, meaning that the riser is much more tensioned than without current velocity applied. After some time, the tension magnitude appears to be very similar.

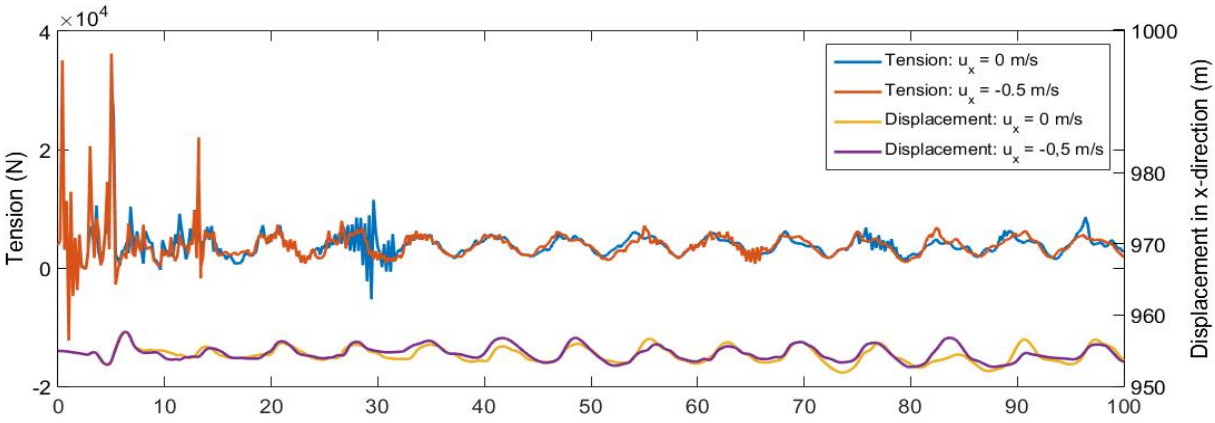

Figure 11 – Displacement and tension in x-direction

Roll angle and regular heave motion

The next situation considers two dynamic steps, first one for roll angles of 6 rad and 9 rad with a ramp of 20 s, and the second one with a duration of 100 s considering a regular heave with amplitude of 2 m and period of 15 s. Once again, the time step was set as automatic, and the minimum value was in the order of 10^{-3} for the torsion simulation, and 10^{-2} for the regular heave simulation.

In this study, the concept of total curvature (Koloshkin, 2016) is introduced, which is given by Eq. (11).

$$\kappa_T = \sqrt{\kappa_y^2 + \kappa_z^2} \tag{11}$$

The maximum total curvature of the structure was calculated by a set of other simulation. It was found that the riser supports curvatures of 0,4405 m^{-1}, and if this value is exceeded, the riser buckles and loop formation occurs.

Figure 12 shows the behavior of the riser during heave, the picks of curvatures exceed the maximum curvature value when the riser is diving into the sea water, meaning that the structure presents loops on the TDZ (Fig 13 – a). In Figure 12-a, the maximum total curvature is not exceeded and after sixteen seconds, tension and curvature show a pattern.

In the case which the riser was tensioned by the heave, the loop was undone and the picks of curvatures decreased (Fig 13 – b). The compression wave was seen on the riser traveling from its touchdown point to its top during negative tension situations. Also, lateral deflections were observed.

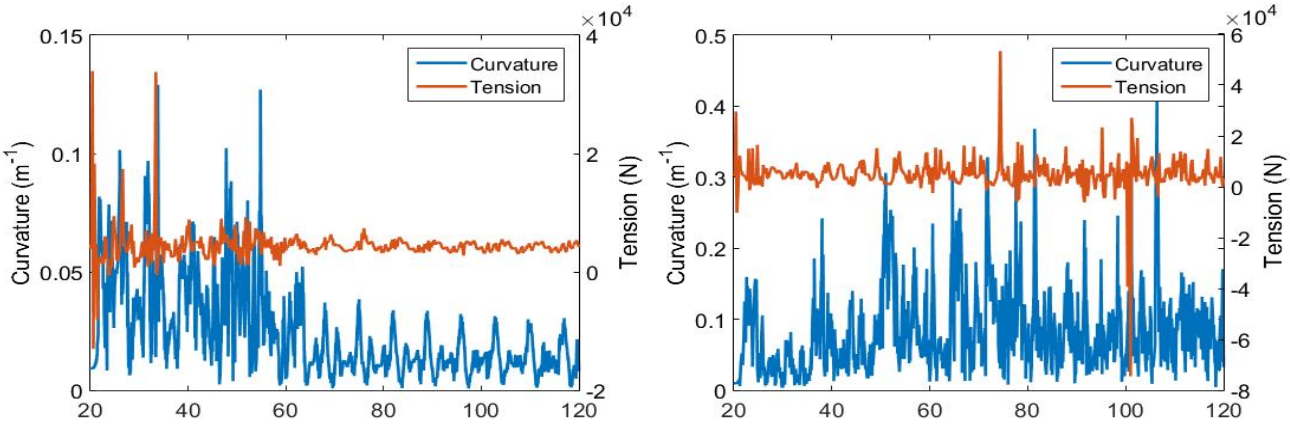

(a) 6 rad (b) 9 rad

Figure 12 – Tension and Curvature for regular heave

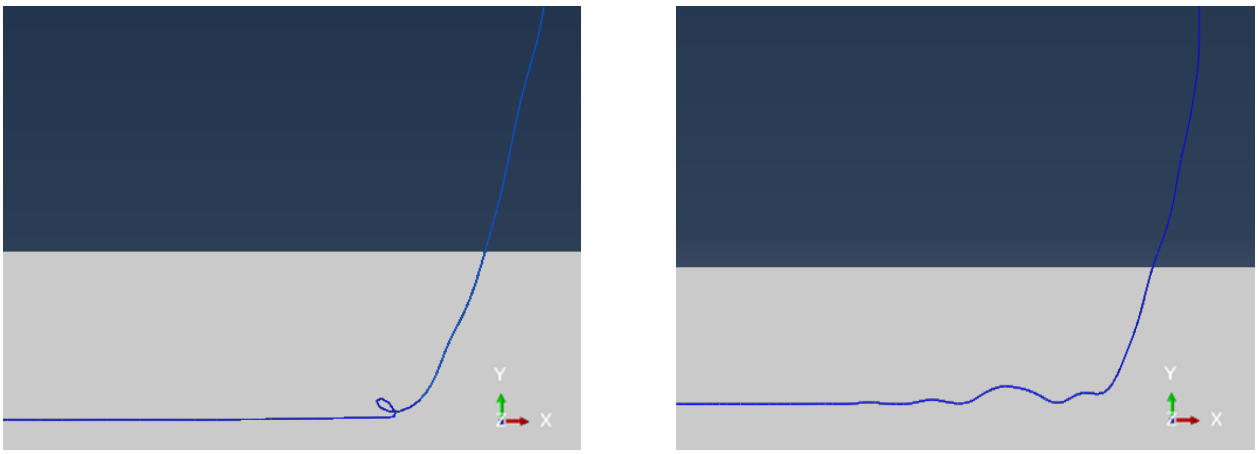

(a) (b)

Figure 13 – Deformed riser with regular heave

Roll angle and irregular heave motion

In this study, a step with a 20 s ramp was applied for the roll angle, and a step of 100 s was used to apply the irregular heave motion with a zero-crossing period of 15 s and significative heights of 2 m and 4 m. The minimum time step found was in the order of 10^{-4} s.

Figure 14 shows the tension and curvature of the riser submitted to irregular waves. During the first two seconds, the tension was very high and curvature small ($H_s = 2\ m$: 300 kN (6 rad) and 600 kN (9 rad). $H_s = 4\ m$: 500 kN (6 rad) and 100 kN (9 rad)), so, for a better visualization of the curve, they where omitted.

The same as before happens with the riser, which presents low curvatures when tensioned (Fig. 15 – a), and when the riser buckles, the maximum curvature is exceeded forming loops (Fig. 15 – b), and consequently kinks.

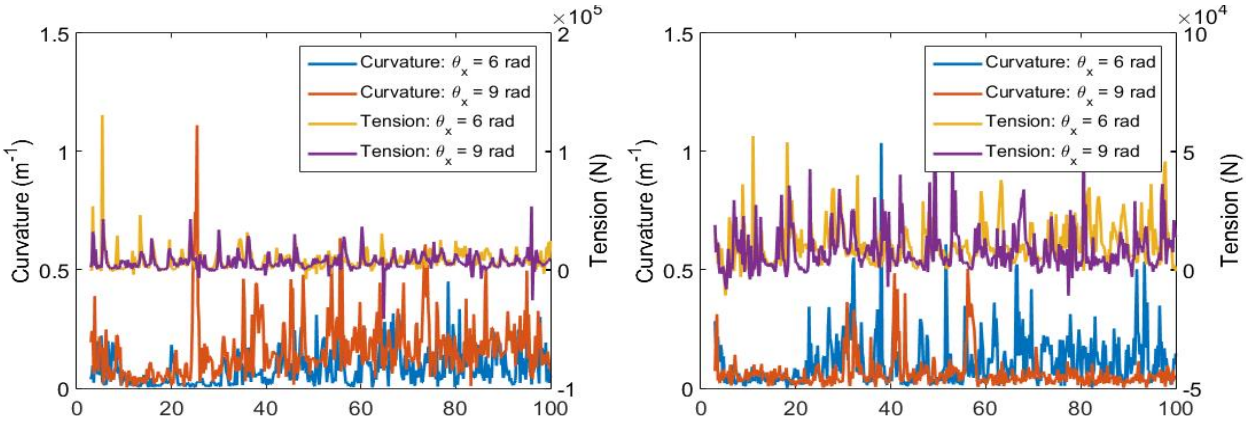

(a) $H_s = 2$ m (b) $H_s = 4$ m

Figure 14 – Tension and Curvature for irregular heave

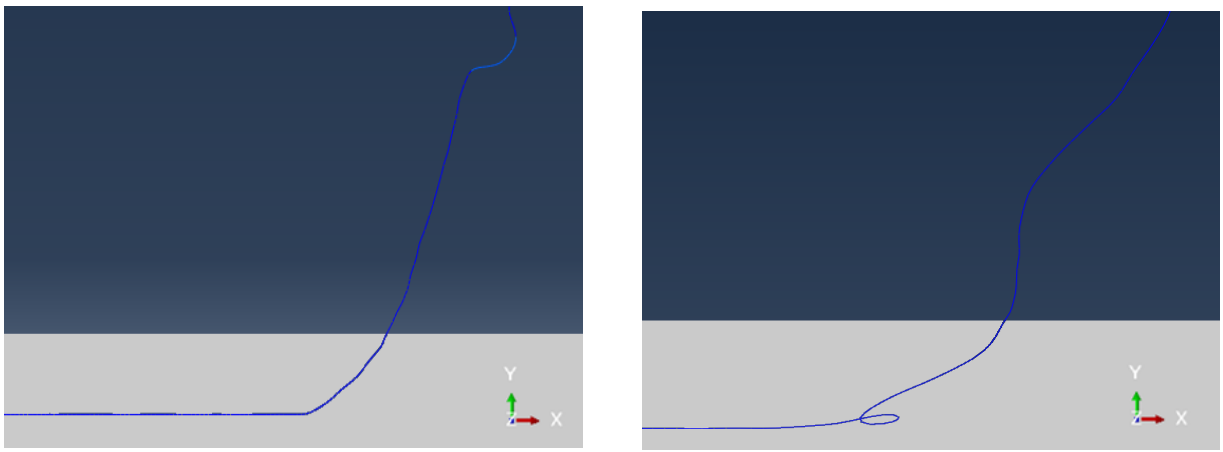

(a) (b)

Figure 15 – Deformed riser with irregular heave

CONCLUSION

The main purpose of this work is to evaluate the effects of torsion and dynamic compression in flexible risers, which can lead to failure of the structure. At first, it was analyzed that the current velocity and the drag coefficient can be considered as hydrodynamic dampers once, the riser response shows smoother movements and are more tensioned. Then, a study on regular heave motion was performed, and it was seen that either heave or roll are equally important to the kink formation analysis.

Finally, the irregular heave motion analysis showed that the riser varies depending on the model of wave. After the imposed torsion, if heave pushes the riser down the sea level, the structure present high compression levels in the touchdown zone, and loops are formed. Also, greatest lateral and axial displacements are given by the combination of great wave heights, great roll angles and small periods.

In both regular and irregular cases, the compression wave was seen in the beginning of the simulations due to the Euler's critical load which was exceeded.

REFERENCES

AMARANTE, R. D. A. "Compressão dinâmica em risers". (PhD Thesis) – University of São Paulo. São Paulo. 2015.

KOLOSHKIN, E. "Torsion buckling of dynamic flexible risers". (Master Thesis) - Norwegian University of Science and Technology. Trondheim. 2016.

LI, S.; SUN, B. Advances in soft matter mechanics. Higher Education Press, pp. 240, 2012.

LITEWKA, P. Finite Element Analysis of Beam-to-Beam Contact. Poznan: Springer, v. 53, 2010.

MIYAZAKI, Y.; KONDO, K. Analytical solution of spatial elastica and its application to kinking problem. "International journal of solids and structures", v. 34, pp. 3619-3636, 1997. ISSN 27

NETO, A. G. "Estabilidade estrutural da configuração estática de risers em catenária". (PhD Thesis) - University of São Paulo. São Paulo. 2012.

RIBEIRO, E. J. B.; ROVERI, F. E.; MOURELLE, M. M. Dynamic Compression Buckling in Flexible Riser. "Offshore Technology Conference", 1998

TAKAFUJI, F. C. D. M. "Dinâmica Tridimensional de Risers". (PhD Thesis). - University of São Paulo. São Paulo. 2010.

YASSERI, R.; SIROUS, ; BIN, W. Integrity of subsea control umbilica. ASME 2014 33rd International Conference on Ocean, Offshore and Arctic Engineering, San Francisco, 2014.

RESPONSIBILITY NOTICE

The author(s) is (are) the only responsible for the printed material included in this paper.

APENDIX

Elastic Stiffness Matrix

$$\mathbf{K}_E = \begin{bmatrix}
\frac{EA}{L} & 0 & 0 & 0 & 0 & 0 & -\frac{EA}{L} & 0 & 0 & 0 & 0 & 0 \\
0 & \frac{12EI}{L^3} & 0 & 0 & 0 & \frac{6EI}{L^2} & 0 & -\frac{12EI}{L^3} & 0 & 0 & 0 & \frac{6EI}{L^2} \\
0 & 0 & \frac{12EI}{L^3} & 0 & -\frac{6EI}{L^2} & 0 & 0 & 0 & -\frac{12EI}{L^3} & 0 & -\frac{6EI}{L^2} & 0 \\
0 & 0 & 0 & \frac{GJ}{L} & 0 & 0 & 0 & 0 & 0 & -\frac{GJ}{L} & 0 & 0 \\
0 & 0 & -\frac{6EI}{L^2} & 0 & \frac{4EI}{L} & 0 & 0 & 0 & \frac{6EI}{L^2} & 0 & \frac{2EI}{L} & 0 \\
0 & \frac{6EI}{L^2} & 0 & 0 & 0 & \frac{4EI}{L} & 0 & -\frac{6EI}{L^2} & 0 & 0 & 0 & \frac{2EI}{L} \\
-\frac{EA}{L} & 0 & 0 & 0 & 0 & 0 & \frac{EA}{L} & 0 & 0 & 0 & 0 & 0 \\
0 & -\frac{12EI}{L^3} & 0 & 0 & 0 & -\frac{6EI}{L^2} & 0 & \frac{12EI}{L^3} & 0 & 0 & 0 & -\frac{6EI}{L^2} \\
0 & 0 & -\frac{12EI}{L^3} & 0 & \frac{6EI}{L^2} & 0 & 0 & 0 & \frac{12EI}{L^3} & 0 & \frac{6EI}{L^2} & 0 \\
0 & 0 & 0 & -\frac{GJ}{L} & 0 & 0 & 0 & 0 & 0 & \frac{GJ}{L} & 0 & 0 \\
0 & 0 & -\frac{6EI}{L^2} & 0 & \frac{2EI}{L} & 0 & 0 & 0 & \frac{6EI}{L^2} & 0 & \frac{4EI}{L} & 0 \\
0 & \frac{6EI}{L^2} & 0 & 0 & 0 & \frac{2EI}{L} & 0 & -\frac{6EI}{L^2} & 0 & 0 & 0 & \frac{4EI}{L}
\end{bmatrix}$$

Geometric Stiffness Matrix

$$\mathbf{K}_G = \begin{bmatrix}
0 & 0 & 0 & 0 & 0 & 0 & 0 & 0 & 0 & 0 & 0 & 0 \\
0 & \frac{6T}{5L} & 0 & 0 & 0 & \frac{T}{10} & 0 & -\frac{6T}{5L} & 0 & 0 & 0 & \frac{T}{10} \\
0 & 0 & \frac{6T}{5L} & 0 & -\frac{T}{10} & 0 & 0 & 0 & -\frac{6T}{5L} & 0 & -\frac{T}{10} & 0 \\
0 & 0 & 0 & 0 & 0 & 0 & 0 & 0 & 0 & 0 & 0 & 0 \\
0 & 0 & -\frac{T}{10} & 0 & \frac{2TL}{15} & 0 & 0 & 0 & \frac{T}{10} & 0 & -\frac{TL}{30} & 0 \\
0 & \frac{T}{10} & 0 & 0 & 0 & \frac{2TL}{15} & 0 & -\frac{T}{10} & 0 & 0 & 0 & -\frac{TL}{30} \\
0 & 0 & 0 & 0 & 0 & 0 & 0 & 0 & 0 & 0 & 0 & 0 \\
0 & -\frac{6T}{5L} & 0 & 0 & 0 & -\frac{T}{10} & 0 & \frac{6T}{5L} & 0 & 0 & 0 & -\frac{T}{10} \\
0 & 0 & -\frac{6T}{5L} & 0 & \frac{T}{10} & 0 & 0 & 0 & \frac{6T}{5L} & 0 & \frac{T}{10} & 0 \\
0 & 0 & 0 & 0 & 0 & 0 & 0 & 0 & 0 & 0 & 0 & 0 \\
0 & 0 & -\frac{T}{10} & 0 & -\frac{TL}{30} & 0 & 0 & 0 & \frac{T}{10} & 0 & \frac{2TL}{15} & 0 \\
0 & \frac{T}{10} & 0 & 0 & 0 & -\frac{TL}{30} & 0 & -\frac{T}{10} & 0 & 0 & 0 & \frac{2TL}{15}
\end{bmatrix}$$

Mass Matrix

$$\mathbf{M} = \frac{\rho AL}{420}\begin{bmatrix}
140 & 0 & 0 & 0 & 0 & 0 & 70 & 0 & 0 & 0 & 0 & 0 \\
0 & 156 & 0 & 0 & 0 & 22L & 0 & 54 & 0 & 0 & 0 & -13L \\
0 & 0 & 156 & 0 & -22L & 0 & 0 & 0 & 54 & 0 & 13L & 0 \\
0 & 0 & 0 & 70R^2 & 0 & 0 & 0 & 0 & 0 & 35R^2 & 0 & 0 \\
0 & 0 & -22L & 0 & 4L^2 & 0 & 0 & 0 & -13L & 0 & -3L^2 & 0 \\
0 & 22L & 0 & 0 & 0 & 4L^2 & 0 & 13L & 0 & 0 & 0 & -3L^2 \\
70 & 0 & 0 & 0 & 0 & 0 & 140 & 0 & 0 & 0 & 0 & 0 \\
0 & 54 & 0 & 0 & 0 & 13L & 0 & 156 & 0 & 0 & 0 & -22L \\
0 & 0 & 54 & 0 & -13L & 0 & 0 & 0 & 156 & 0 & 22L & 0 \\
0 & 0 & 0 & 35R^2 & 0 & 0 & 0 & 0 & 0 & 70R^2 & 0 & 0 \\
0 & 0 & 13L & 0 & -3L^2 & 0 & 0 & 0 & 22L & 0 & 4L^2 & 0 \\
0 & -13L & 0 & 0 & 0 & -3L^2 & 0 & -22L & 0 & 0 & 0 & 4L^2
\end{bmatrix}$$

Added Mass Matrix

$$\mathbf{M}_a = \frac{c_a \rho_a A L}{420} \begin{bmatrix} 0 & 0 & 0 & 0 & 0 & 0 & 0 & 0 & 0 & 0 & 0 & 0 \\ 0 & 156 & 0 & 0 & 0 & 22L & 0 & 54 & 0 & 0 & 0 & -13L \\ 0 & 0 & 156 & 0 & -22L & 0 & 0 & 0 & 54 & 0 & 13L & 0 \\ 0 & 0 & 0 & 0 & 0 & 0 & 0 & 0 & 0 & 0 & 0 & 0 \\ 0 & 0 & -22L & 0 & 4L^2 & 0 & 0 & 0 & -13L & 0 & -3L^2 & 0 \\ 0 & 22L & 0 & 0 & 0 & 4L^2 & 0 & 13L & 0 & 0 & 0 & -3L^2 \\ 0 & 0 & 0 & 0 & 0 & 0 & 0 & 0 & 0 & 0 & 0 & 0 \\ 0 & 54 & 0 & 0 & 0 & 13L & 0 & 156 & 0 & 0 & 0 & -22L \\ 0 & 0 & 54 & 0 & -13L & 0 & 0 & 0 & 156 & 0 & 22L & 0 \\ 0 & 0 & 0 & 0 & 0 & 0 & 0 & 0 & 0 & 0 & 0 & 0 \\ 0 & 0 & 13L & 0 & -3L^2 & 0 & 0 & 0 & 22L & 0 & 4L^2 & 0 \\ 0 & -13L & 0 & 0 & 0 & -3L^2 & 0 & -22L & 0 & 0 & 0 & 4L^2 \end{bmatrix}$$

Irregular Wave Components

	$H_s = 2m$		$H_s = 4m$	
ω (rad/s)	φ (°)	Amplitude (m)	φ (°)	Amplitude (m)
0.1	55	0	56	0
0.2	200	4.65E-12	316	2.32E-12
0.3	70	0.001451	249	0.000725
0.4	66	0.113996	294	0.056998
0.5	181	0.443342	219	0.221671
0.6	20	0.648189	2	0.324095
0.7	200	0.642692	8	0.321346
0.8	31	0.552973	118	0.276487
0.9	203	0.453801	173	0.226901
1	79	0.368324	49	0.184162
1.1	64	0.299882	352	0.149941
1.2	221	0.246247	239	0.123124
1.3	294	0.204293	292	0.102146
1.4	142	0.17127	252	0.085635
1.5	179	0.145031	2	0.072515
1.6	261	0.123962	235	0.061981
1.7	283	0.106866	267	0.053433
1.8	9	0.092852	358	0.046426
1.9	325	0.081253	73	0.040627
2	293	0.071569	169	0.035784
2.1	161	0.063414	255	0.031707
2.2	81	0.056496	300	0.028248
2.3	356	0.050585	146	0.025293
2.4	270	0.045501	292	0.022751
2.5	2	0.041103	158	0.020551
2.6	333	0.037275	236	0.018638
2.7	161	0.033928	17	0.016964
2.8	161	0.030986	356	0.015493
2.9	52	0.028388	237	0.014194
3	66	0.026085	161	0.013042